Multimodal and Non-Linear Optical Microscopy Applications in Reproductive Biology

J. ADUR,[1,2,3]* G.O. BARBOSA,[4] V.B. PELEGATI,[1,5] M.O. BARATTI,[5] C.L. CESAR,[1,5,6] V.H. CASCO,[2,3] AND H.F. CARVALHO[4,5]

[1]*Biophotonic Group. Optics and Photonics Research Center (CEPOF), Institute of Physics "Gleb Wataghin," State University of Campinas, Brazil*
[2]*Biofotónica y Procesamiento de Información Biológica (ByPIB), CITER - Centro de Investigación y Transferencia de Entre Ríos, CONICET-UNER, Argentina*
[3]*Microscopy Laboratory Applied to Molecular and Cellular Studies, School of Bioengineering, National University of Entre Ríos, Argentina*
[4]*Department of Structural and Functional Biology, Biology Institute, State University of Campinas, Brazil*
[5]*INFABiC - National Institute of Science and Technology on Photonics Applied to Cell Biology, Campinas, Brazil*
[6]*Department of Physics of Federal University of Ceara (UFC), Brazil*

KEY WORDS optical workstation; confocal platform; multifoton microscopy; nonlinear microscopy

ABSTRACT A plethora of optical techniques is currently available to obtain non-destructive, contactless, real time information with subcellular spatial resolution to observe cell processes. Each technique has its own unique features for imaging and for obtaining certain biological information. However none of the available techniques can be of universal use. For a comprehensive investigation of biological specimens and events, one needs to use a combination of bioimaging methods, often at the same time. Some modern confocal/multiphoton microscopes provide simultaneous fluorescence, fluorescence lifetime imaging, and four-dimensional imaging. Some of them can also easily be adapted for harmonic generation imaging, and to permit cell manipulation technique. In this work we present a multimodal optical workstation that extends a commercially available confocal microscope to include nonlinear/multiphoton microscopy and optical manipulation/stimulation tools. The nonlinear microscopy capabilities were added to the commercial confocal microscope by exploiting all the flexibility offered by the manufacturer. The various capabilities of this workstation as applied directly to reproductive biology are discussed. *Microsc. Res. Tech. 79:567–582, 2016.*

INTRODUCTION

Until recently, most of the knowledge about cell biology events has been obtained through statistical inference on large sample observations. However, researchers learned that cells are adaptive devices, which change their behavior constantly both in time and space, with huge cell-to-cell heterogeneity. Cells divide and change behavior during their lifetime and also respond to external physiological and stressing stimuli. Moreover, often, a deeper analysis of cells whose behavior is beyond the average tissue environment, provide novel ideas or scenarios for research or a relevant diagnostic whose detection would be impossible in standard studies. Therefore, efforts to put together to achieve highly sensitive, real time, non-destructive, chemically sensitive single cell observations, are strongly dependent on non-destructive high-resolution optical techniques.

Today there is a plethora of isolated accessories to collect non-destructive, contactless, real time information with subcellular spatial resolution to observe cellular and molecular phenomena. In the 1980's, Optical Tweezers (OT) were developed and used to manipulate and measure biomechanical properties of cells, membranes, and organelles (Ashkin et al., 1986). In the early 1990's, with the appearance of femtosecond Ti:sapphire lasers, the possibilities for Multiphoton Microscopy was demonstrated (Denk et al., 1990). Deeper penetration was one of the major advantages of Multiphoton Microscopy and became almost mandatory for *in vivo* studies. Simultaneously, the Fluorescence Lifetime Imaging Microscopy (FLIM) reached enormous progress in both time domain and frequency domain (König et al., 1996). By the late 1990's two powerful non-linear techniques were developed: second harmonic generation (SHG) and Coherent Anti-Stokes Raman Scattering (CARS) (Campagnola et al., 1999; Zumbusch et al., 1999). They used essentially

*Correspondence to: J Adur, Biofotónica y Procesamiento de Información Biológica (ByPIB), CITER - Centro De Investigación y Transferencia de Entre Ríos, CONICET-UNER, Argentina; and H.F. CARVALHO, Department of Structural and Functional Biology, Biology Institute, State University of Campinas, Brazil. E-mail: jadur@bioingenieria.edu.ar and hern@unicamp.br

Received 27 November 2015; accepted in revised form 4 May 2016

REVIEW EDITOR: Dr. Peter Saggau

Contract grant sponsor: FAPESP; Contract grant number: 2009/16150-6 (to H.F.C.); Contract grant sponsor: FAPESP; Contract grant number: 2011/51591-3; Contract grant sponsors: CEPOF (Optics and Photonics Research Center, FAPESP), INFABIC (National Institute of Photonics Applied to Cell Biology, FAPESP and CNPq), PICTO UNER-INTA-CAFEGS; Contract grant number: 2009-209; Contract grant sponsor: PIO CONICET-UNER Res: 4337/15; Contract grant number: N° 14620140100004 CO).

DOI 10.1002/jemt.22684
Published online 24 May 2016 in Wiley Online Library (wileyonlinelibrary.com).

the same multiphoton apparatus but counted with different laser sources. SHG microscopy allowed the selective visualization of collagen fibers and fibrils, acto-myosin filaments and microtubules, while CARS microscopy allowed chemically selective imaging, particularly of lipids. In the last years researchers discovered that third harmonic generation (THG) microscopy is also capable of providing images due to variations in the third order susceptibility $\chi 3$, or refractive index and other inhomogeneities (Débarre et al., 2005). Each of these imaging techniques has its own imaging possibilities and provides distinct biological information. However, none of these techniques can be of universal use. For a comprehensive investigation of biological events on a given sample, we designed an integrated-multimodal photonic platform.

One such multimodal microscope was implemented by a combination of THG, SHG, and Multi-photon Excited Fluorescence (MPEF) image contrast methods (Gualda et al., 2008). Similarly, we combined two photon-excited fluorescence (TPEF), SHG, and THG in the same platform (Adur et al., 2011). Other important confocal setups modified for harmonic generation were reported (Carriles et al., 2009; Cox et al., 2005; Sun et al., 2004; Sun, 2005). However, these home built systems lacked the FLIM modality. In 2012, we reported the development of an easy-to-operate platform capable to perform TPEF, SHG, THG, and FLIM using a single 80 MHz femtosecond Ti:sapphire laser source (Pelegati et al., 2012). A recent review presents relevant publications in the field of multimodal nonlinear imaging microscopy techniques (Meyer et al., 2013). In that work, some examples shows the combination of four techniques, such CARS, SHG, TPEF, and Optical Coherence Tomography (OCT) (Tang et al., 2012) and CARS, SHG, THG, and TPEF (Tsai et al., 2012) to analyze tumor progression. Also, last year we presented how combine (TPEF, SHG, THG, and CARS) techniques in one setup to improve the accuracy of multimodal nonlinear images in the detection of epithelial cancers. In the same work we reviewed the significant advances in new technologies used in nonlinear microscopy, i.e., laser sources, scanning systems and detectors (Adur et al., 2014a).

Presently, we are working to integrate more than four techniques in the same microscopy setup. In this work, we review the concept "multimodal" and present our own new multimodal optical setup. In the first part, the different microscopy and manipulation cell techniques are presented. Also, we discuss aspects of the instrumentation involved in nonlinear microscopy (the general layout for a multimodal microscope). The second part presents applications of TPEF, SHG, THG, CARS, FLIM and OTs in reproductive biology and some examples of this technique used in intravital experience.

MULTIMODAL CONTRAST MECHANISMS

In microscopy, the "multimodal" term means that we can observe and analyze images captured using different microscopy techniques. For example, in a confocal microscope, if the energy density at the focal spot of the objective lens is sufficiently large, nonlinear optical effects such as harmonic generation (SHG, THG), CARS, parametric oscillations, and multi-photon fluorescence can be observed (Fig. 1). These optical phenomena are used in combination to study a given biological specimen simultaneously (Adur et al., 2011; Gualda et al., 2008).

Nonlinear optical effects occur when a biological tissue interacts with an intense laser beam and exhibits a nonlinear response to the applied field strength (Carriles et al., 2009). Table 1 summarizes the unique features of each nonlinear optical imaging contrast mechanism. TPEF is a third-order non-linear optical process where two photons excite an electron from the ground state. It is an inelastic process releasing photon energy in the sample. Two-photon absorption happens only when the energy of the incident photons fall into the two-photon excitation band which is specific for each fluorescent compound. The two-photon excitation band is not exactly half of the one photon excitation band because the selection rules are different. The fact that TPE depends on the square of the incident light provides optical sectioning, because it can only happen in the focal point volume. On the other hand, the emission is an incoherent optical process with a lifetime that depends not only on the excited molecule, but also on the chemical environment around it. Photobleaching is smaller in TPEF compared to single photon excitation because the excited volume is smaller. Therefore, TPEF allow the observation of specific molecules, by selecting both, the excitation and emission wavelength, and by determining different fluorescence lifetimes (Cella and Diaspro, 2010).

In contrast, SHG and THG are coherent second/third-order elastic nonlinear optical processes. Because two/three photons generate another photon with two/three times the energy of the incident photons (Fig. 1), there is no energy release to the medium, meaning that no infocus cell photodamage is expected from these processes, although there is always a damage threshold intensity, or fluency, for ultrafast laser pulses due to multiphoton ionization. Both SHG/THG can be isolated from fluorescence by either the wavelength or time gating, because the coherent processes are instantaneous in practical terms. Given that SHG signal is proportional to I^2 and THG signal is proportional to I^3, where I is the incident light intensity, they intrinsically provide optical sectioning. For the same wavelength of the incident light, THG has better optical sectioning resolution than SHG. One practical problem with THG is the fact that the emitted light wavelength falls in the UV-blue range of the spectrum and become resonant with biological molecules electron level transitions, with higher absorption. Besides, scattering also increases in the UV-blue range, hence and light penetration is reduced (Carriles et al., 2009; Pelegati et al., 2012).

Selective SHG cancellation due to central symmetry has been observed in several biologically relevant systems including lipid vesicles infused with styryl dye, sarcomeric anisotropic bands in muscle cells, and plant starch granules (Moreaux et al., 2000; Prent et al., 2008). In biological materials containing well organized in non-centrosymmetric microcrystalline structures, the SHG from different emitters adds coherently resulting in very intense SHG. Some examples of such structures include starch granules and other plant polysaccharides, collagen, striated muscle,

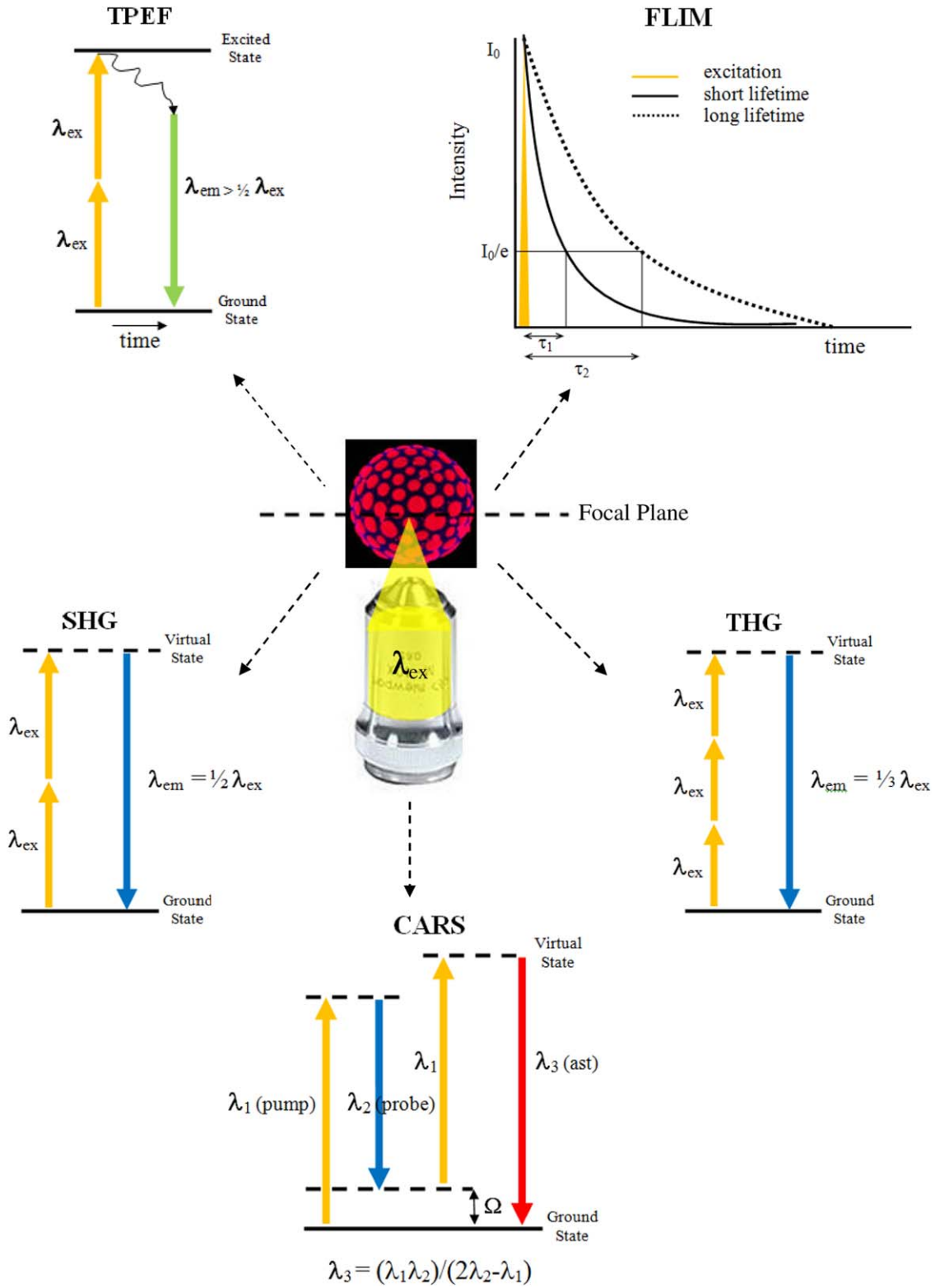

Fig. 1. Jablonski diagrams depicting TPEF, SHG, THG, and CARS nonlinear microscopy techniques, as well as the principle of time-domain fluorescent lifetime. TPEF combines energy of two photons to excite one molecule to an excited state, which subsequently proceeds along the fluorescence emission pathway. TPEF is widely used to image fluorescence. SHG combine photons of equal energy to generate new photons with combined energy. SHG is sensitive to non-centrosymmetric biological structures including collagen fiber and microtubule. THG combines photons of equal energy to form new photons with triple the energy. THG is dependent on optical heterogeneities of probed objects, which include third-order non-linear susceptibility, refractive index, and refraction. CARS is a four-wave mixing process, where molecular vibration frequency Ω is equal to $1/\lambda_1^{-1}/\lambda_2$. If Ω matches Raman-active band of CH_2 at 2840 cm^{-1}, vibrational contrast of lipid-rich structures is generated. By using FLIM, the fluorophores are excited using a short laser pulse after which emitted photons are measured over time. Depending upon the fluorophore and environmental conditions, the fluorescence lifetime will be distinct and in many cases, multiple components may exist for the fluorophore. [Color figure can be viewed in the online issue, which is available at wileyonlinelibrary.com.]

TABLE 1. Features of nonlinear optical microscopy using various nonlinear optical phenomena

Features	TPEF	FLIM	SHG	THG	CARS
Susceptibility	χ^3	χ	χ^2	χ^3	χ^3
Discovery in optics	1961	1989	1961	1962	1965
Application into bioscience	1990	1996 with SHG	1986	1997	1982
Advantages	-Deeper imaging with less photobleaching. -Spatial localization for Fluorescence excitation. -Intrinsic fluorescence from NADH, flavins, and fluorescent proteins.	-Different fluorophores with the same emission band can be discriminated by their fluorescence lifetimes, which enhances the specificity of fluorescence observations. -more reliable quantification of FRET	-Coherent process, symmetry selection. -Probing well-ordered structures, functions of membranes, Non fluorescent Tissues.	-Coherent process, no symmetry requirement. -Imaging both in bulk and at surfaces for extended conjugation of pi electrons.	-Coherent process. -Inherent vibrationalcontrast for the cellular species, requires no endogenous or exogenous fluorophores. -Vibrational and Chemical sensitivities.
Disadvantages	- lack of sensitivity to structural information - heat release	- more acquisition time requirements - Specific analysis software requirements	-noncentrosymmetric microenvironment requirements	- special concerns with UV wavelength if IR excitation lower of 1000 nm is used - difficult to detect	- difficult to implement - complementary technique - limited signal-to-noise
Applications	-Depth imaging in brain slices, combined with disease models and fluorescence indicators.	- Sensitive to the chemical microenvironment around the fluorophores such as pH, ion, and oxygen concentration	-Structural protein arrays, collagen-related diseases, membrane potential with styryl dyes.	-General cells and tissues, developmental biology neuroscience	C-H stretching band, amide I band, phosphate stretching band in cells and tissues.
Laser Sources	-Tunable Ti:sapphire laser over 700–1000 nm with pulse width of 100 femtoseconds	-Tunable Ti:sapphire laser over 700–1000 nm with pulse width of 100 femtoseconds	Tunable Ti:sapphire laser over 700–1000 nm with pulse width of 100 femtoseconds	Optical parametric oscillator (OPO), Cr:forsterite at 1230 nm	Picosecond Ti:sapphire laser, OPO, Nd:vanadate at 1064 nm

χ (electric susceptibility): is a dimensionless proportionality constant that indicates the degree of polarization of a dielectric material in response to an applied electric field. This can be (χ): linear electric susceptibility [dimensionless] or (χ^n): nonlinear electric susceptibility $[m/V]^{n-1}$ that appear at very high values of electric field (ex: pulsed laser). Photobleaching: the photochemical alteration of a dye or a fluorophore molecule. TPEF: two photon excited fluorescence, FLIM: fluorescence lifetime imaging microscopy, SHG: second harmonic generation, THG: third harmonic generation, CARS: coherent anti-stokes raman scattering, FRET: Förster resonance energy transfer, NADH: reduced nicotinamide adenine dinucleotide.

and chloroplasts (Chu et al., 2001; Campagnola and Yuan-Dong, 2011). THG have been used to monitor embryo development and mitosis in zebra fish (Chu et al., 2003; Sun et al., 2004) and to observe human glial cells (Barille et al., 2001), cardiomyocytes (Barzda et al., 2005), green algae rhizoids (Squier et al., 1998), chloroplasts (Muller et al., 1998), erythrocytes (Millard et al., 1999), epithelial, neuronal, muscle cells (Yelin et al., 2002), and intracellular Ca^{2+} dynamics (Canioni et al., 2001). Our experience with both techniques to study cancer tumors is that SHG is extremely useful to observe collagen networks in the extracellular space, while THG can display clearly the nuclei, two very important information for pathologists (Adur et al., 2011, 2012a,b).

CARS microscopy derives its imaging contrast from Raman-active vibrational modes and has been used for cellular and tissue imaging. CARS relies on the contrast resulting from probing resonances of specific chemical bonds in unstained samples, enabling its chemical selectivity. In brief, when the energy difference, Ω, (Fig. 1) between the pump and probe (also called the Stokes beam in the Raman literature) matches the energy gap, ω_v, of a particular vibrational transition, $\Omega \equiv \omega_{pump} - \omega_{probe} \rightarrow \omega_v$, then the (difference frequency) beating between the pump and probe beams drives the vibrational oscillators within the focus coherently in phase. Its coherent nature further renders CARS signal several orders of magnitude stronger than the conventional Raman signal, thus offering video-rate imaging speed (Evans et al., 2005). Therefore, this imaging modality has been successfully applied to a variety of biomedical applications, including the imaging of viruses, cells, tissues and live animals (Huff and Cheng, 2007; Krafft et al., 2009; Le et al., 2009; Mouras et al., 2010). Unlike SHG and CARS, for tightly focused laser beams, a THG signal is only generated when the medium is optically heterogeneous (both linearly and/or nonlinearly) within the focal volume scale. Recently, it was demonstrated that THG microscopy can reveal the presence of lipid bodies within thick tissue and be efficiently combined with multiphoton fluorescence and SHG microscopy (Gualda et al., 2008). Thus, based on different contrast mechanisms for the different techniques (TPEF, FLIM, SHG, THG, CARS), the simultaneous application of these is expected to reveal valuable and complementary information about the tissue under investigation (Meyer et al., 2013).

On the other hand, all living cells face mechanical forces that are converted into biochemical signals and integrated into the cellular responses (mechanotransduction). Therefore, the development of new techniques for exerting mechanical stresses on cells and for observing their responses is crucial to clarify the molecule- and cell-level structures that may participate in mechanotransduction. Forces can be exerted on a cell by a variety of experimental techniques. If the force is in the right range of magnitude, it is capable of eliciting a biological response from the cell. The level of force needed to produce a significant conformational change in the force-transmitting proteins can be estimated. Several studies have measured the fibronectin/integrin binding strength, producing estimates in the range of 30–100 pN. Forces as low as 3–5 pN have also been shown to be sufficient to unfold certain subdomains in fibronectin. Interestingly, this is also the range of forces exerted on the particle in an optical trap by the radiation pressure of light.

In 1986, Ashkin discovered that a single, tightly focused laser beam could be used to capture small dielectric particles and confine them three-dimensionally (Ashkin et al., 1986). An OT system consists of a laser beam tightly focused into a very small region, generating an extremely large electric field gradient, using a microscope objective. When such a tightly focused laser beam interacts with a mesoscopic particle, piconewton forces are exerted on the particle and it is attracted toward the highest intensity region by the so-called gradient force, while the radiation force, also known as the scattering force, acts in the direction of the light propagation. Under the conditions when the gradient force dominates, the particle with a refractive index larger than that of the surrounding medium is trapped in three dimensions. For this reason, OTs are usually constructed with a microscope objective (Gu et al., 2010).

This relatively young technique provides the non-mechanical manipulation of biological particles such as viruses, living cells, and subcellular organelles. OTs are now being used in the investigation of an increasing number of biochemical and biophysical processes, from the mechanical properties of biological polymers to the multitude of molecular machines that drive the internal dynamics of the cell (Galla et al., 2014; Khatibzadeh et al., 2014; Pesce et al., 2014, 2015; Spyratou et al., 2014). OTs are compatible with fluorescence-imaging techniques. Therefore, it is possible to apply localized mechanical and chemical stimuli on cells while following changes in cell shape and organization. The combination of chemical and mechanical stimulation is useful and relevant in cell biology, since cells test the extracellular matrix (ECM) rigidity during their differentiation. Furthermore, OTs open the field for a single molecule manipulation and its biophysical characterization. With the appropriate chemistry, a bead can be attached to a single molecule as a handle allowing the application of forces on a single molecule. In conclusion, OTs microscopy can be used for a wide range of experiments, from the single molecule to the cell level and helps to understand their organization up to the tissue level (Heller et al., 2014; Moura et al., 2015).

MULTIMODAL MICROSCOPE ARCHITECTURE

The engineering challenge is to integrate the different modalities on a single platform. In response to this challenge, manufacturers have designed microscopes with multiple input and output ports and increased infinity space for the introduction of customized optics. Nonlinear microscopes share many common features with confocal laser scanning microscopes. In fact, many research groups have implemented multiphoton excitation fluorescence by coupling optical parametric oscillators (OPO), femtosecond or picosecond lasers into a confocal scanning microscope (Cox et al., 2005; Plotnikov et al., 2006) and by using a nondescanned port for efficient detection of the nonlinear signal.

For example, Cheng and Sun, described a typical imaging system for multi-modal, nonlinear microscope

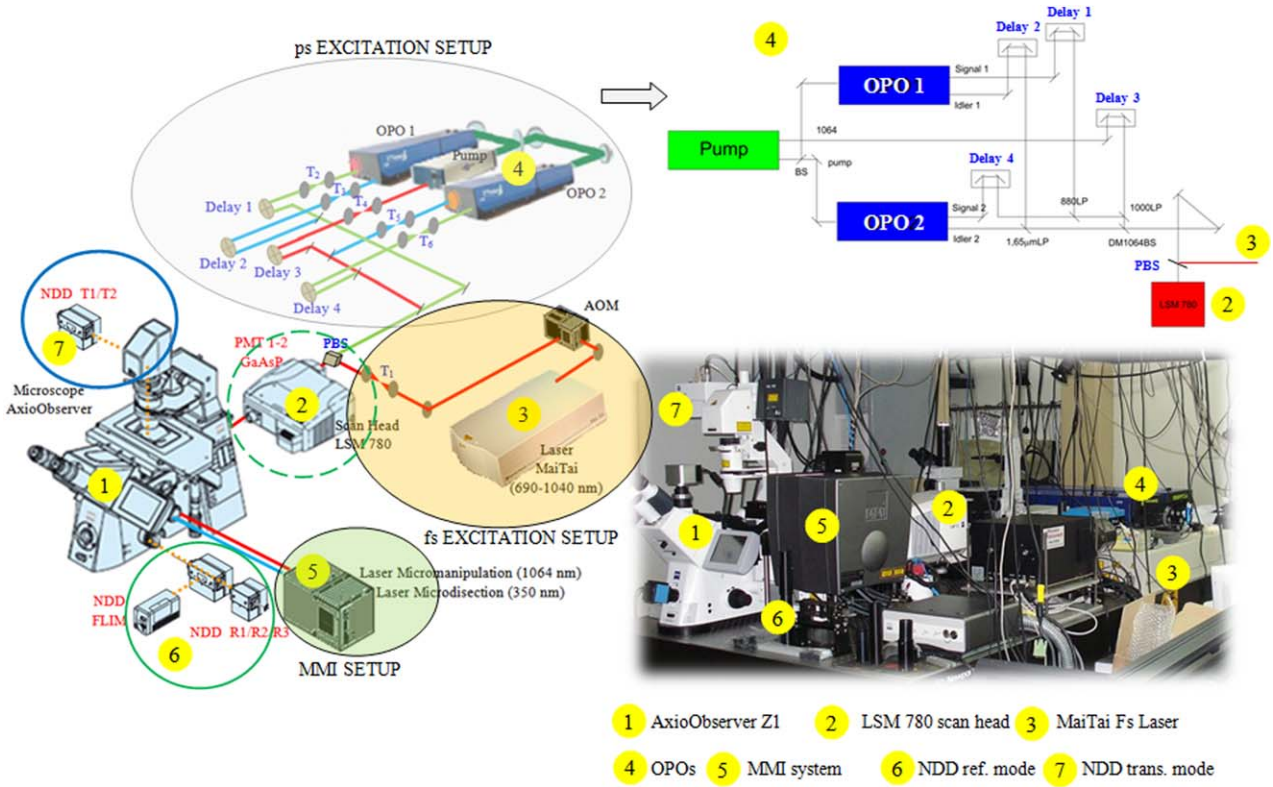

Fig. 2. Schematic diagram of a multimodal NLO microscope setup built at INFABIC (UNICAMP). Femtosecond (MaiTai) and picoseconds (OPOs system) pulsed laser and lasers for microdissection and micromanipulation are couple to a commercial confocal system platform (inverted Zeiss Axio Observer.Z1 and confocal LSM 780). Shaded circles show excitation sources whereas circle with dashed lines, the detection configurations. The upper right panel depicts a more detailed picoseconds excitation setup. Pump (Nd:YVO-laser (HighQ laser)), OPOs (APE, Levante Emerald), BS (50:50 beamsplitter. EdmundOptics ID 2757). Three reflection mirrors (532 nm, EdmundOptics ID 2765). The each five wavelengths (signal and idler for each OPO plus the fundamental 1064 nm) are independently controlled with a half wave plate and PBS (not shown). Delay lines (two lens: Newport KPX094AR.16 and Newport KPX082AR.16). AOM: acousto-optic modulator. Principal optic elements are shown in blue. T: Telescope Lens, Detectors are shown in red. NDD T: Non Descanned Detector - transmitted way, NDD R: Non Descanned Detector - reflective way, NDD FLIM: Non Descanned Detector - reflective FLIM, PMT: photomultiplier tubes. Solid line: excitation path, Dashed line: emission path. [Color figure can be viewed in the online issue, which is available at wileyonlinelibrary.com.]

using either Cr:forsterite, Nd:glass, ytterbium, or Ti:Sa lasers. Briefly, the laser beam is conducted with a spatial filter and collimated by a beam expander to fill the back aperture of the objective lens. The beam was coupled into an Olympus IX71 microscope through the confocal scanning unit with a 45° dichroic beamsplitter to reflect the infrared (IR) and transmit visible light. The excitation IR light was focused onto the biological sample with a spot size close to diffraction limit using high numerical aperture (NA) objectives and the excited photoemission spectrum was collected using an opposing high-NA objective. The collected light (visible and near IR) is then directed into a spectrometer and recorded by a Peltier-cooled charge-coupled device (CCD) detector. Transmission detection was used because most SHG and THG is emitted in the forward direction (Cheng and Sun, 2006). Alternative constructions using different combinations of techniques have been published (Adur et al., 2014a; Carriles et al., 2009; Gualda et al., 2008; Mathew et al., 2009; Saager et al., 2015).

Figure 2 shows a schematic setup of a multimodal microscope built at the National Institute of Science and Technology on Photonics Applied to Cell Biology (INFABIC) at the State University of Campinas (UNICAMP), on a commercial confocal system platform (inverted Zeiss Axio Observer.Z1 and confocal laser scanning microscopy LSM 780).

Excitation Sources: The system has ultraviolet (UV)-lamp, five continuous-wave (CW) lasers for confocal modality, pulsed lasers - picoseconds (ps) and femtoseconds (fs) - for nonlinear studies and other two CW laser - ultraviolet (UV) and IR - for microdissection and micromanipulation respectively. UV-lamp (X-cite® 120 Excelitas Technologies) is for classical epifluorescence observation. The five lines of CW laser (Argon (458, 488, 514 nm) 35 mW, HeNe (543 nm) 1 mW, and HeNe (633 nm) 5 mW) are coupled to the scan head (LSM 780 visible laser ports) through polarization-preserving single-mode optical fibers (not show in Fig. 2). One variable beam collimator for each beam provides optimum adaptation of the respective laser wavelength to the objective used and assures the same focal plane for all laser lines.

The picosecond source comes from a synchronously pumped OPO system (APE, Levante Emerald) to acquire high spectral resolution CARS microscopy. The master oscillator is a picosecond mode-locked frequency

doubled Nd:YVO-laser (HighQ laser) operating at 1064 nm with a second amplification stage followed by a frequency doubler crystal capable to deliver more than 8W of green output power at 532 nm. A polarizing beam splitter (PBS) separates the fundamental at 1064 nm from the second harmonic at 532 nm, which is equally divided to pump two OPOs (See Fig. 2: shaded gray and upper right panel). Each individual OPO uses a temperature-tuned, noncritically phase-matched LBO (LiB_3O_5) crystal for parametric down conversion. The temperature of the crystal sets the wavelengths of the two generated near IR signal and idler synchronized in time, but with a time delay because the two beams are separated in a dichroic filter and exits at two different ports. The OPO can be easily and continuously tuned over a wide spectral range, from 690 to 990 nm for the signal, and between 1150 and 2300 nm for the idler output. Automated tuning is performed via computer control. This system is capable to provide five different wavelength beams, the fundamental at 1064 nm, two signals and two idlers, one for each OPO. The power of these five wavelength beams are controlled independently with a half wave plate and PBS (not shown); their time overlapping is obtained by using four independent delay lines (Newport Optical-Delay-Line-Kit/396220/1033), and the spatial superposition in the focal plane is obtained by the use of dedicated telescopes/collimators (T2, T3, T4, T5, and T6) composed by two lens (lens 1: Plano-Convex Lens, BK 7, 25.4 mm diameter, 100 mm EFL, 650-1000 nm and lens 2: Plano-Convex Lens, BK 7, 25.4 mm diameter, 50.2 mm EFL, 650-1000 nm-Newport).

The femtoseconds laser source is a tunable Ti:sapphire laser (Spectra-Physics Mai Tai®) with 2W output, at the repetition rate of 80 MHz, emitting around 690-1040 nm for efficient TPEF, FLIM or for higher SHG/THG harmonics generation. The beam is coupled to the scan head through an acousto-optic modulator (AOM) for a fast intensity control and with a collimating telescope (T_1) to adjust both the beam diameter to fill the objective back-aperture of the objective and the beam focus position on the microscope focal plane (See Fig. 2: shaded orange). We merged the ps OPO with fs Ti:sapphire, both operating in the same wavelength range, in one collinear beam with a PBS, sent onto the backward excitation port of the scan head (LSM 780 IR laser port). This way we obtained a wavelength independent beam splitter, which send the fs beam in one polarization and the ps one in the other polarization.

For microdissection and micromanipulation the MMI CellCut/CellManipulator (Molecular Machines & Industries, AG) system was coupled in the left part of the AxioObserver microscopy (See Fig. 2: shaded green). This system specially designed optics focuses the laser beam without impairing any functionality of the inverted microscope. Laser microdissection is performed with a 355nm laser, and the regions of interest (ROI) for microdissection are selected in a touch screen. The OTs use a 1064 YAG infrared laser with 3W trapping power that can be split (time-share mode) to trap up to 10 different objects. The final power at the sample is less than 200 mW that allows living cells studies.

For alternative configurations the readers can refer to Chen and Brustlein works, where Mai Tai® laser and one OPO (Opal-BB, Spectra-Physics) on FV1000 Olympus confocal systems is shown (Chen et al., 2009) or different possible configurations starting with one OPO and two OPOs (APE, Levante Emerald) on a Nikon C1-Si system (Brustlein et al., 2011).

Signal Detection

The motorized collimators, the scanners, the precise pinhole position and the highly sensitive detectors are selected to provide optimum specimen illumination and efficient collection of the emitted light. The generated signals (reflected or epi-detection) can be collected with the same microscope objective (high-NA C-APOCHROMAT especially developed to reach the physical limit in resolving power and used throughout the 380. . .900 nm spectral range), split by dichroic mirrors, which were specifically chosen for the given fundamental and fluorescence or harmonic emission wavelengths and focused onto specific detectors. To efficiently block near IR excitation stray light from the detector, special TwinGate (narrow angle geometry) main dichroic beam splitters (MBS) are used (MBS 690+: main dichroic beam splitter reflecting near IR excitation longer than 690 nm, transmitting shorter wavelengths) in the light path. Interference or band pass filters are used in front of the detector for filtering spurious signals outside the desired bandwidth.

Detection in the backward direction: the scan head of the LSM780 (See Fig. 2: green circle with dashed lines) has a spectral GaAsP Quasar detector (Quiet Spectral Array) with 32 in-line elements (spectral detection range freely selectable -resolution down to 3 nm-) actively cooled (45% of Quantum Efficiency) plus 2 adjacent photomultipliers tube (PMT) (400-700 nm detection range) that expand the spectral working collection (not show). In addition, three cascade non-descanned detectors (NDD) with GaAsP NDD unit are available for epi-detection of nonlinear signals (NDD R1/R2/R3). In the same setup we can exchange any NDD by detectors for FLIM signal (HPM-100 GaAsP hybrid detector based on Hamamatsu R10467, Becker & Hickl GmbH) using C-mount adapter (See Fig. 2: green circle with solid lines). These detectors combine high time resolution, high efficiency, large area, and easy alignment.

Detection in the forward direction: the microscope's transmitted-light channel is equipped with a PMT, too. It is therefore possible to superimpose a multiple fluorescence image on a brightfield, differential interference or phase contrast image. Additionally, two NDD with GaAsP NDD unit are used in transmission path (NDD T1/T2) (See Fig. 2: blue circle with solid lines). If NDD channels are assigned to the transmitted-light beam path, no transmission PMT can be implemented.

Signal Acquisition, Control and Software

Our optical setup is principally controlled by ZEN software from Carl Zeiss. The software run on dedicated computer and is used to control the microscope, the scanning module, the laser module, and the image acquisition process display, edit and analyze the images. The Laser Control tool of ZEN shows the nonlinear optics (NLO) laser as an additional laser of the system. The wavelength and laser intensity are

controlled in the laser control pop up from the Light Path tool. The desired wavelength is chosen in the Edit Laser Wavelength input box. Non-Descanned Detection is set and configured in the Light Path tool by choosing the Non-Descanned tab next to the LSM tab. The configuration of multiple tracks is possible for NDD applications, but they cannot be combined with tracks which are set up with the standard channels.

In other computers we control FLIM and micromanipulation modalities. FLIM acquisition setup is performed using SPCM Data Acquisition Software. After setting the parameters, NLO laser bottom is checking and automatic FLIM acquisition start. SPCImage software is used for FLIM data analysis. Both, acquisition and analysis software are providing by Becker & Hickl GmbH. For MMI system, the MMI CellTools software V. 2011 is used. Its graphical user interface allows the precise and intuitive identification and selection of the areas of interest. With same software, even the automated microscope functions such as objective changes, condenser settings and fluorescence turret changes can be initiated.

OPERATIONAL FUNCTIONS AND APPLICATIONS

Multimodal Capabilities

In this review, a nonlinear/multiphoton microscopy system based on a commercial confocal microscope is presented. All the flexibility offered by the basic setup (3D fluorescence, time lapse, laser-scanning bright-field, DIC, and spectral separation) were fully exploited, to which were added: NND forward and backward detection systems, separate backward FLIM detectors, and manipulation tools with separate control systems and software. The new functions were incorporated without altering any of the components of the LSM 780 microscope. These improvements give it the following capabilities:

1. Simultaneous TPEF and SHG, or TPEF and THG, or SHG and THG forward imaging
2. Simultaneous TPEF and SHG forward and TPEF and SHG backward imaging
3. Simultaneous SHG and CARS imaging
4. Option 1 + sequentially FLIM imaging
5. Optical trapping + sequentially CARS and SHG or FLIM or Option 1

To display the flexibility of the system, a set of illustrative studies of our group on different reproductive organs are showed.

A. Multimodal Images of Breast and Ovarian Tissues. Figure 3 depicts representative NLO images of ovary and breast human tissues obtained from normal (Fig. 3A) and cancer (Fig. 3B) thin section ($\sim$ 5μm) samples stained with Hematoxylin & Eosin (H&E). These organs were imaged by using TPEF (green color) and FLIM (map blue to red color) to visualize intrinsic fluorophores, SHG (red color) to visualize collagen, THG (magenta color) to highlights the nuclei, and CARS (map red to yellow color) to visualize lipids. Forward THG signals and backward TPEF and SHG signals were simultaneously collected with NDD, whereas backward FLIM and CARS signals were sequentially recorded. From TPEF, SHG and THG excitation wavelength was 940 nm. The THG signal (313 nm) that strongly highlights the nuclei is detected with a band-pass BP340 ± 30 nm colored glass filter (Hoya Corporation). The SHG (470 nm) corresponds to stromal collagen and is detected with a filter cube with a dichroic long-pass LP490 nm wavelength and a filter short-pass SP485 nm. The TPEF signal (> 500 nm) corresponding to eosin fluorescence (Carvalho and Taboga, 1996) was strong outside the nuclei but weaker inside, being detected by using other filter cube with a mirror and a narrow (20 nm FWHM) BP540 filter. From FLIM images (unstained, but fixed, samples), that show weighted mean fluorescence lifetime (τ_m), excitation was 890 nm, which excites mainly the flavin adenine dinucleotide (FAD) fluorescence (Huang et al., 2002). FLIM signal is detected with a filter (LP) E-690- HP (Omega Filters) used to reflect the TPEF/FLIM signal to a fast detector (Becker & Hickl, PMH-100). Time-correlated single photon counting (TCSPC) card electronics (Becker & Hickl, SPC-830) allowed the direct TPEF image acquisition, which was later processed to obtain the FLIM images in the time domain. The FLIM images provide more information and allow the correlation of the lifetime to these different structures. Blue and red colors represent short and long fluorescence lifetimes respectively. Because SHG is an instantaneous NLO process it also appears in the FLIM images like a very fast lifetime component (blue color). For CARS imaging of lipids, the pump laser (fs laser) at 790 nm (12,658 cm^{-1}) and the Stokes laser (OPO) at 1018 nm (9823 cm^{-1}) provides a wavenumber difference centered at 2,840 cm^{-1} that matches the Raman shift of the symmetric CH_2 stretch vibration in lipids. The CARS signal at 645 nm was detected by the internal spectral detectors in the segment windows of 620–670 nm. These results shows that the structural information revealed by each nonlinear contrast mechanism can be isolated and analyzed separately with this system, while their superimposition allows a better comparison and understanding of the spatial organization of the tissue.

Even more important, we have previously shown that these setup capabilities can be used to detect morphological and metabolic changes associated with stroma and epithelial transformation during the progression of cancer (Adur et al., 2011; Adur et al., 2012a,b). Figure 3B, shows a few examples were, NLO microscopes provide complementary information about tissue microstructure, depicting distinctive patterns for different types of human mucinous ovarian and breast cancer tumors. In the first case, we have simultaneously used SHG and THG and sequentially FLIM techniques to analyze adenoma and borderline ovarian tissues, which were then compared with normal tissue. From the THG + SHG merged image epithelial/stromal interface was easily identified. In these images, collagen fibers with different orientations and distribution can be clearly identified by the SHG signal (red color) in the stroma region. In normal samples we found that collagen fibers were more linearly arranged with long, straight fibrils, whereas the collagen of abnormal samples exhibits a loss of fine structure and structural organization. Different quantitative tools can be used to analyze orientation and distribution of collagen fibers (Adur et al., 2014c; Tilbury and

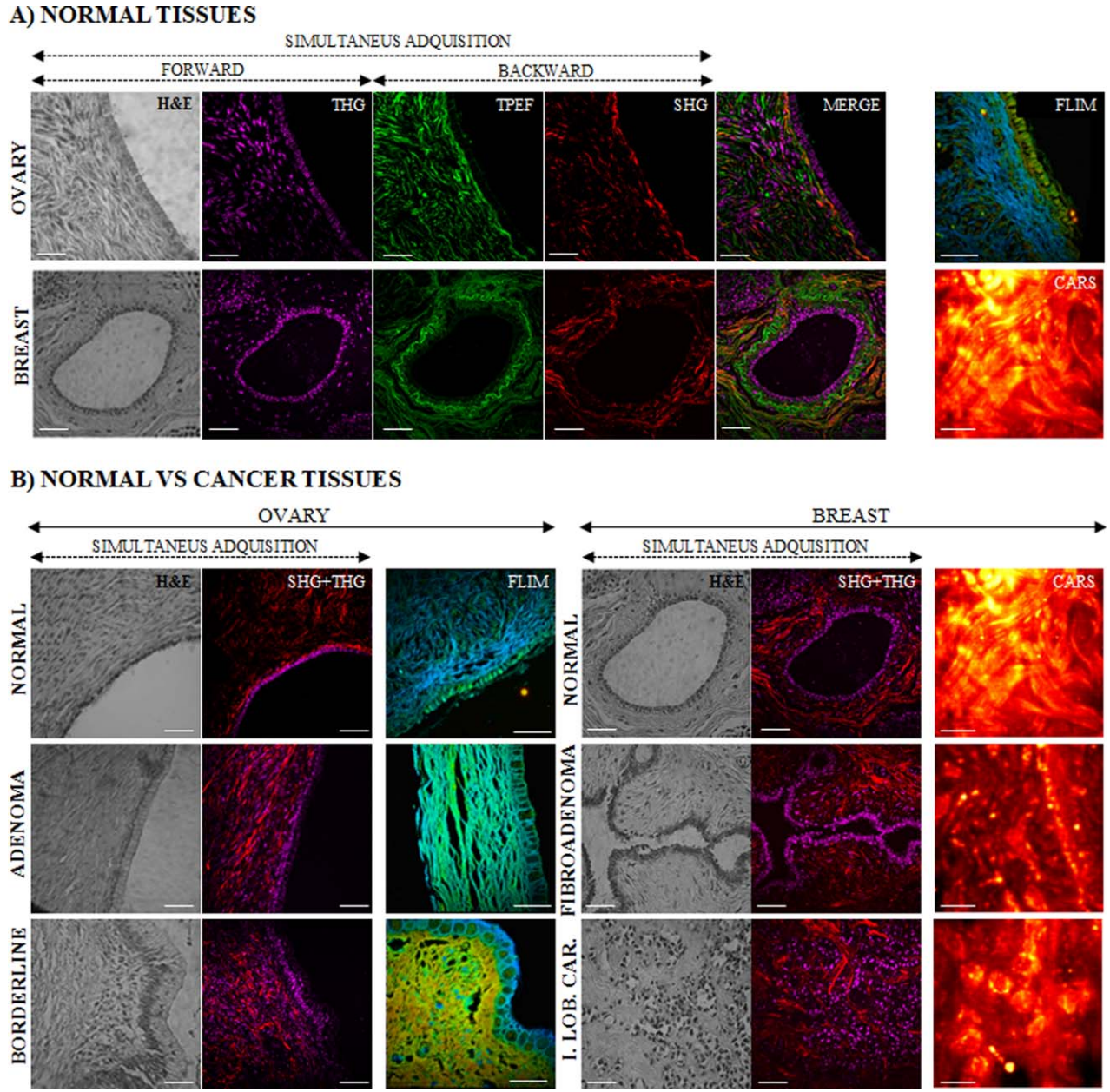

Fig. 3. Representative –(A) normal and (B) normal vs cancerous tissues– multimodal cross-sectional images of H&E-stained ovary and breast samples for: SHG (red), THG (magenta), CARS (map red to yellow color) analyses, and unstained samples for FLIM (map blue to red color) study. For TPEF, SHG and THG the excitation wavelength was 940 nm. The THG (313 nm), SHG (470 nm), and TPEF (> 500 nm) signals were detected with specific filters (see the text body). From FLIM images, that show weighted mean fluorescence lifetime (τ_m), excitation was 890 nm. In mucinous ovarian human tissues, the color map of FLIM images represents the τ_m of the two-term model components $\tau_m = (a_1\tau_1 + a_2\tau_2) / (a_1 + a_2)$. Blue and red colors represent short and long fluorescence lifetimes respectively. For CARS imaging, the pump laser (fs laser) at 790 nm (12658 cm^{-1}) and the Stokes laser (OPO) at 1018 nm (9823 cm^{-1}) provides a wavenumber difference centered at 2840 cm^{-1} that matches the Raman shift of the symmetric CH_2 stretch vibration in lipids. All images were obtained with 40X/1.30 NA oil immersion C-APOCHROMAT lens. All scale bars = 20 μm. Abbreviations: I. Lob. Carc: Invasive lobular carcinoma. Figures from Adur et al., 2012a; Adur et al., 2012b (open access); Adur et al., 2014a. [Color figure can be viewed in the online issue, which is available at wileyonlinelibrary.com.]

Campagnola, 2015). We have probed in previous works (Adur et al., 2012b,b) that the lower spatial frequencies increased, whereas the higher spatial frequencies decreased in the cancer group compared with the non-diseased group, consistent with an alteration in collagen fibril fine structure (reduction of higher spatial frequencies) in the cancer group as was also previously presented by Kirkpatrick and Willians group's (Kirkpatrick et al., 2007; Williams et al., 2010). Moreover, using the same signal we previously quantified the collagen fiber angle relative to the epithelium. Specifically, we find straightened (taut) collagen fibers

stretched around the epithelium in normal and adenoma samples; and identification of radially aligned collagen fibers that facilitate local invasion in borderline and adenocarcinoma ones (Adur et al., 2011, 2014b). From THG (magenta color) we can qualitatively recognize differences in surface epithelium of each tumor type. In previous reports, using THG signal, we presented an automatic quantitative evaluation of the quantity of nuclei and the epithelial width to assess epithelial transformations (Adur et al., 2011). Our results correlate well with quantifications previously performed on H&E stained sections from the same tumor types (Scully et al., 1998). FLIM allowed us to use cellular FAD as an endogenous biomarker to estimate cell metabolism (Adur et al., 2012b; Huang et al., 2002; Skala et al., 2007). Differences in fluorescence lifetime of FAD between different epithelial cells are color mapped. Epithelial cells of borderline tissues showed a longer fluorescent lifetime (orange color) compared with normal and benign samples (blue/green color), allowing epithelial cells of malignant ovary to be easily differentiated from epithelial cells of healthy ovary. By using FLIM, similar to previous reports (Conklin et al., 2009; Provenzano et al., 2009; Skala et al., 2007), we measured in previous work an increase in the fluorescence lifetime for FAD in tumor cells (Adur et al., 2012b).

Regarding breast tissues, we simultaneously used SHG, THG, and sequentially CARS images to differentiate between normal and malignant [Fibroadenoma and Invasive Lobular Carcinoma (ILC)] human breast tissue. Characteristic microscopic appearance of each type of tissue, and relationship between cells and stroma can be identified, in the SHG/THG combination. Based on these multicontrast images we evaluated recently collagen-related changes by anisotropy and determined texture features calculations (Adur et al., 2014a). As expected, malignant breast tissues present higher entropy that usually implies elevated levels of disorder and disorganization. In a comparative analysis of CARS images of breast tissue, adipose and fibrous structures of normal tissue possess strong CARS signals. Fibroadenoma exhibits the compressed duct with linear branching pattern whereas ILC present single or cell rows invading into the stroma. Based on examples like this, and our previous works (Adur et al., 2012a) we have established that it is possible to have both qualitative and quantitative parameters of differences between each kind of breast tumor and to demonstrate the advantage of the integration of as many NLO approaches as possible to analyze breast human cancer.

In summary, our data demonstrated that different scoring methods extracted from images obtained with a multimodal platform of NLO microscopy techniques are useful to detect pathological changes associated with cancer progression.

B. Multimodal Images of Intra-Vital Mouse Breast Images. Figure 4 shows other example where the setup is used to study live mouse mammary gland with intra-vital microscopy (IVM) technique. This is used to visualize and analyze cell-ECM interactions, angiogenesis, cell migration, cell contraction, metastasis, etc. (Baron et al., 2011). The main advantages of IVM include the real-time analysis of dynamic processes with single-cell resolution. We examined during several hours a broad field of a single gland (Fig. 4A.2), capturing sequentially images with FLIM (Fig. 4A.1) and simultaneously TPEF + SHG (Fig. 4A.3) techniques. With this setup we were able to observe epithelial cells by autofluorescence (cyan color) in TPEF and with a long fluorescence lifetime (orange/red color) in FLIM acquisition. On the other hand, collagen fibers were observed using SHG (red), exhibiting a short fluorescence lifetime (blue) with FLIM. With this configuration we could to analyze the contraction behavior of epithelial cells after oxytocin hormone spraying (Figs. 4B and 4C). These data show (see white arrow) that the dynamic of the epithelial cells contraction, can be analyzed with excellent resolution using intravital two-photon microscopy. In addition to examining the contraction of epithelial cells and traction of collagen fibers in real time with TPEF + SHG after oxytocin treatment, it is possible to verify changes inside cell (FLIM signal), which might suggest mechanical environmental changes (data not shown). However, good FLIM signals require about 60 seconds of acquisition, limiting real-time observations.

C. Multimodal Images of the Prostate Gland. We have reported before that castration promotes striking changes in the stromal compartment, which adjusts to a reducing volume of the gland acini. These changes involve both cells (Antonioli et al., 2004, 2007; Vilamaior et al., 2005) and the ECM (Augusto 2008; Bruni-Cardoso et al., 2010a; Vilamaior et al., 2000). Among this latter, collagen fibers undergo marked reorganization and their intimate contact with the smooth muscle cells (SMC) suggested that these cells were at least in part responsible for the reorganization of the collagen fibers (Vilamaior et al., 2000). This prompted us to observe the dynamics of the ECM in general, and collagen fibers in particular, in the highly dynamic environment of the developing prostate. Our first attempt was to characterize the distribution of Matrix Metalloproteinases (MMPs) in the gland during the first week after birth, considering that the rodent prostate gland experience one important step of development immediately after birth up to the 21st day. This study revealed the particular distribution of MMP-2 and MMP-9 in the developing (Bruni-Cardoso et al., 2008). We then tested the role of MMP-2 using siRNA (Bruni-Cardoso et al., 2010b) and compared the observed changes with those seen in the MMP-2 knockout mouse (Bruni-Cardoso et al., 2010c). For the first time we used SHG to characterize the distribution and content of collagen after MMP-2 knocking down.

New observations using SHG and two-photon excitation of the prostate gland during development showed that collagen fiber deposition occurs in a proximo-distal fashion, as seen in the live organ in culture. While most fibers are aligned in this same direction, some fibers surround the epithelial cords in the proximal region (Fig. 5). SMC differentiate around the epithelium, paralleling the deposition of collagen fibers. One marked observation is the fact that the SMC layer around the growing epithelial structures show blunt ends, revealing a sharp transition in differentiation, as revealed by immunohistochemistry against smooth muscle myosin heavy chain (MYH11) (Fig. 6A). These results reveal that, collagen fiber deposition takes

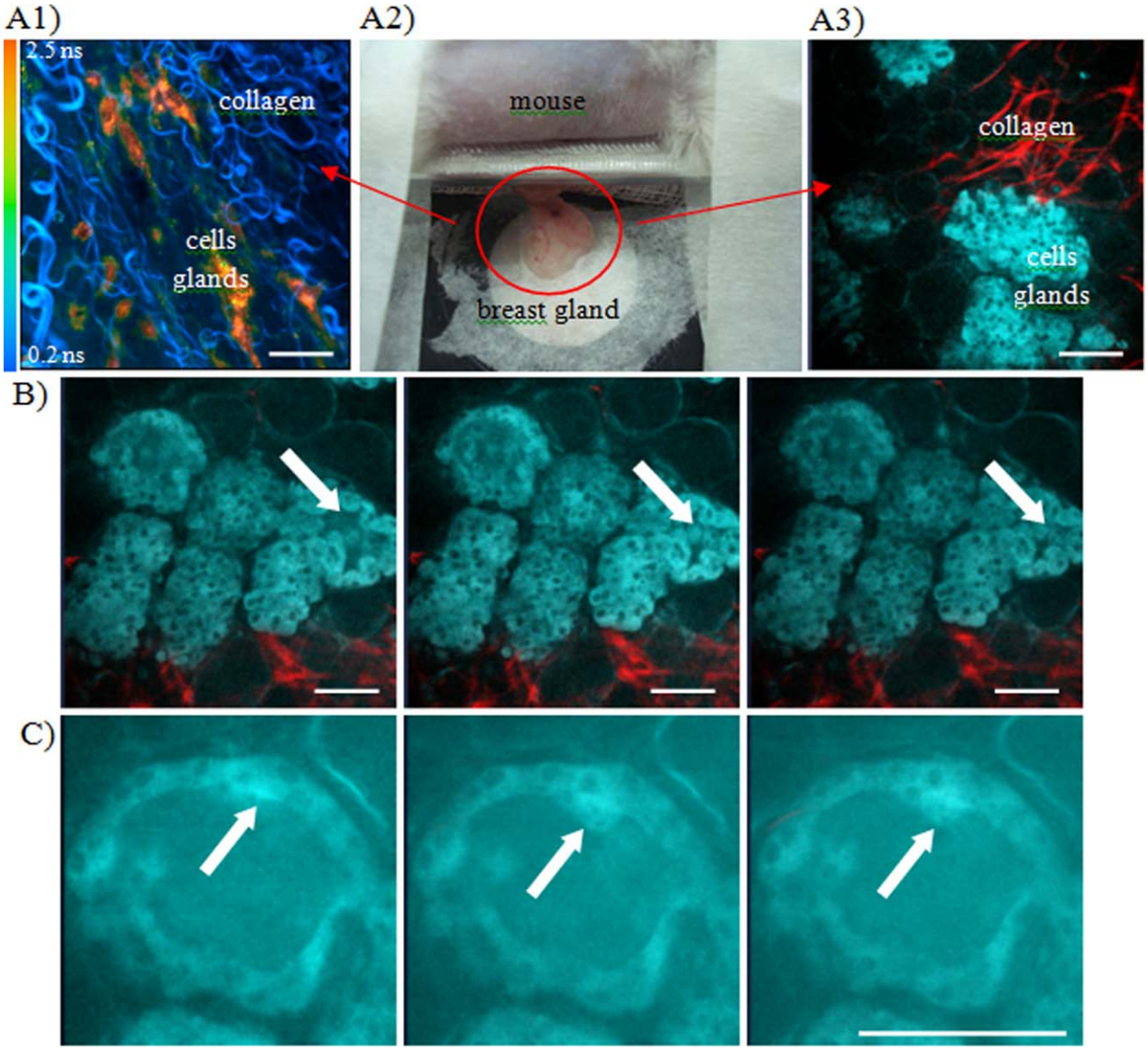

Fig. 4. Intra-vital microscopy (IVM) setup used to study live mouse mammary gland. A broad field of a single gland was examined during several hours (Fig. 4A.2), capturing sequentially images with FLIM (Fig. 4A.1) and simultaneously TPEF + SHG (Fig. 4A.3) techniques at 890 nm. Figure 4A.1 shows FLIM image, blue and orange colors represent lower and higher fluorescence lifetime, respectively. SHG is also visualized by the FLIM detection channel, because to the choice of the emission filter. SHG is an instantaneous nonlinear optical process which, therefore, appears as a very fast lifetime component (blue). In contrast, epithelial cells exhibit lifetime values around 0.5 to 2.5 ns (yellow/orange) which match FAD endogenous fluorophore emission. FLIM signals were collected during 60 seconds at selected intervals. Figure 4A.3 depicts simultaneously TPEF (cyan) + SHG (red) images. With this configuration we were able to analyze the contraction behavior of epithelial cells after oxytocin hormone spraying (Figs. 4B and 4C). These data show (see white arrow) that the dynamic of the epithelial cells contraction, can be analyzed with excellent resolution using intravital two-photon microscopy. Images were obtained with 40X/1.30 NA oil immersion C-APOCHROMAT lens. Scale bars = 50 μm. [Color figure can be viewed in the online issue, which is available at wileyonlinelibrary.com.]

place immediately after SMC differentiation. Additional observations using multiple labeling revealed new aspects of the relationship between collagen deposition, SMC differentiation and epithelial growth. One unique aspect of this complex interaction is that SMC differentiation takes place along the elongating epithelial cords (labelled with anti-cytokeratin 19) and that the blunt border of differentiation is perfectly aligned with the transition between the cord and the growing epithelial tips (labelled by FITC-conjugated tomato lectin) (Fig. 6B). These observations align quite well with the exclusion of SMC from the epithelial outgrowths seen at the 6th-7th postnatal week, in response to the rising testosterone levels associated with puberty (Vilamaior et al., 2005), and the exclusion of myoepithelial cells from the growing buds of mammalian gland organoids in culture (Ewald et al., 2008). We are now addressing the this subject at the cell communication level, trying to identify the mutual interactions responsible for the SMC differentiation at the front of

smooth muscle layer, at the growing tip-cord transition, in parallel with the role of differentiated SMC in collagen deposition.

D. Multimodal Images of Sperm Cells. Fish, insect and goat sperm cells, were analyzed using NLO techniques and the setup described in Figure 2. Figure 7 shows representative images obtained from goat sperm cells. Briefly, samples were cryogenically frozen (Harper et al., 1998) and thawed in a water bath (37°C) for approximately 1 min. Following, samples were transferred to an Eppendorf tube and centrifuged. Supernatants were removed and the remaining sperm pellet suspended in 1mL of pre-warmed media [1 mg of bovine serum albumin (BSA) per 1 mL of Biggers, Whittens, and Whittingham (BWW)]. Since this media is non-capacitating; therefore the sperm do not achieve hyperactivity. To obtain sperm cells images with reasonable signal/noise and minimize errors arising from cell movements, we used OTs to immobilize them. Unstained sperm were head trapped under constant power (460 mW) for a constant duration (90s). During this time, sequentially TPEF, CARS and FLIM images were collected with a small shift between acquisitions. Nice autofluorescence signals were obtained during 5 seconds using 890 nm of excitation allowing the cells identification (head and tail were well defined). Next, the pump laser at 790 nm and the Stokes laser at 1018 nm were set to identify lipid-rich structures with CARS modality. Interestingly, different signals were detected between head and tail of the sperm cells. Finally, FLIM acquisition was performed approximately during 60 seconds using 890 nm of excitation, which was optimal to excite two-photon fluorescence of FAD (Skala et al., 2007). Last year, Reinhardt group's shows that sperm metabolism can be characterized using fluorescence lifetime imaging and that variation in mean fluorescence lifetime may, therefore, be used to compare sperm metabolic properties in males and females (Reinhardt et al., 2015). Also, other reports showed that FAD and reduced nicotinamide adenine dinucleotide (NADH) have an important role in cell metabolism, and their relative presence is used to characterize the redox states of sperm (Miyata et al., 2011; Ribou and Reinhardt, 2012). By using our system, we were able to perform FLIM analysis of FAD and NADH simultaneously. The autofluorescent molecules FAD and NADH could be excited with 760-780 nm wavelengths, emitting at 510-530 and 440-470 nm, respectively. If both components are present, intermediate emission peaks are expected. Under longer excitation wavelengths, a spectral shift towards

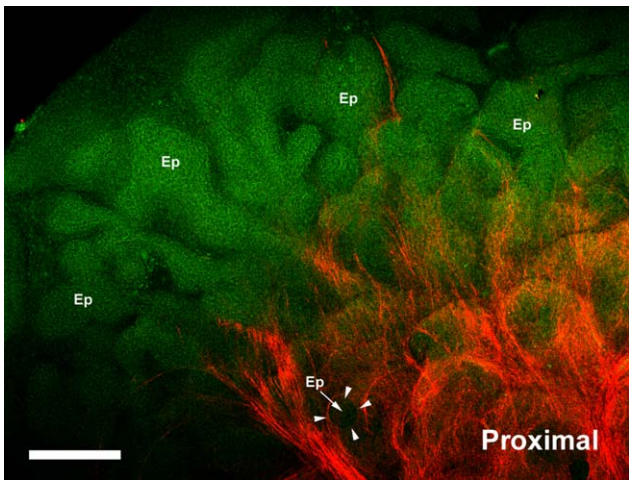

Fig. 5. Imaging of collagen fibers using SHG (red) along with the epithelial structures (mostly epithelial cords) (Ep) detected by the tissue autofluorescence (green) in a living rat ventral prostate kept in culture for 6 days. Collagen accumulation occurs in a proximo-distal direction (with respect to the urethra). A large fraction of the epithelium, including the epithelial tips are devoid of collagen. In the proximal region, collagen fibers are deposited around the epithelial cords/ducts (arrowheads). Maximum intensity projection. Images were obtained with 63X/1.40 NA oil immersion C-APOCHROMAT lens. Bar = 100 μm. [Color figure can be viewed in the online issue, which is available at wileyonlinelibrary.com.]

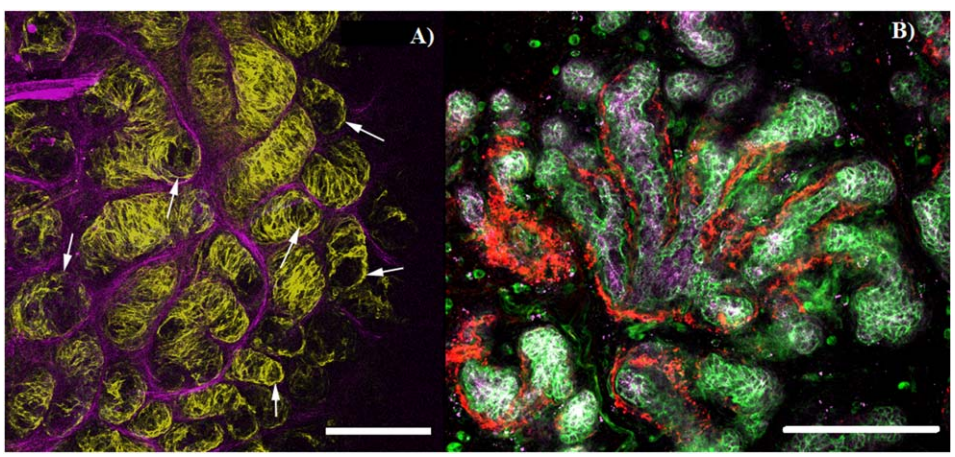

Fig. 6. (A) High resolution view of the interaction between collagen fibers identified by SHG (purple) and smooth muscle cells (SMC) (revealed immunohistochemistry against the smooth muscle myosin heavy chain (MYH11) (yellow), showing the intimate contacts between the two. The figure also reveals the blunt end of SMC differentiation (arrows) around the epithelial structures in the center. Bar = 100 μm. (**B**) Triple staining with antibodies anti-cytokeratin 19 (purple) and anti-SMC myosin heavy chain (red) and with the tomato lectin (green). Optical sections of the gland, arrows point to the blunt transition of SMC differentiation and its coincidence with the tip-cord transition in the epithelium. Bar = 200 μm. Images were obtained with 63X/1.40 NA oil immersion C-APOCHROMAT lens. [Color figure can be viewed in the online issue, which is available at wileyonlinelibrary.com.]

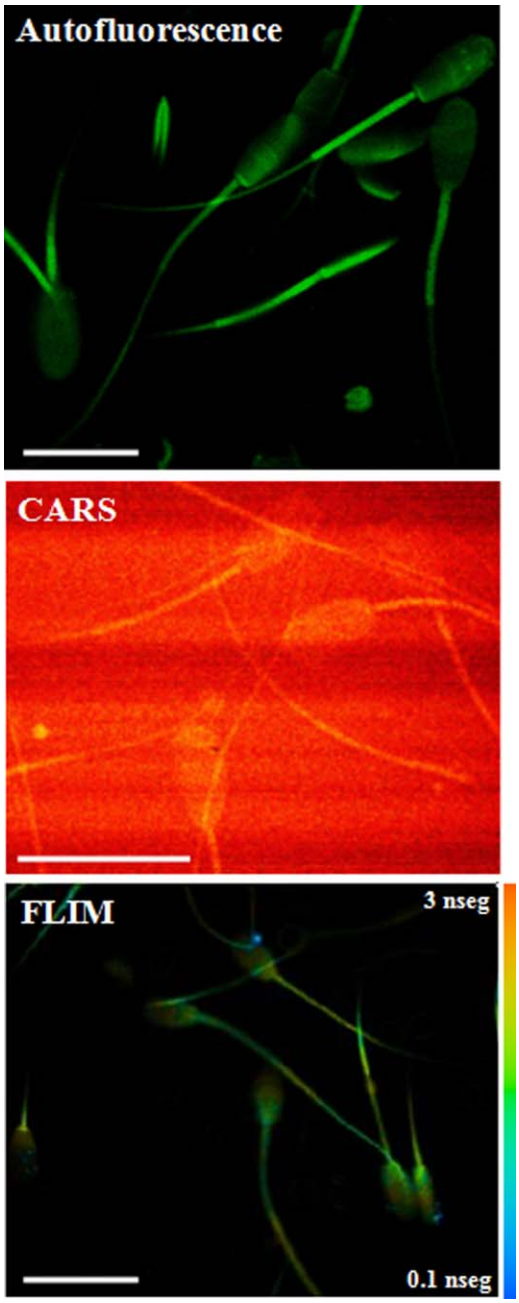

Fig. 7. Goat sperm cells multimodal images. Unstained sperms were head trapped under constant power (460 mW) for a constant time window (90s). During this time, sequentially TPEF, CARS and FLIM images were collected with a small shift between acquisitions. Nice autofluorescence signals were obtained during 5 seconds by using 890 nm of excitation, allowing the cells identification (head and tail were well defined). Next, the pump laser at 790 nm and the Stokes laser at 1018 nm were set to identify lipid-rich structures with CARS modality. Interestingly, different signals were detected from sperm cell's head and tail. Finally, FLIM acquisition was performed approximately during 60 seconds using 890 nm of excitation, which was optimal to excite two-photon fluorescence of FAD. This signal can be used to analyze sperm metabolism. Images were obtained with 40X/1.30 NA oil immersion C-APOCHROMAT lens. Scale bars = 20 μm. [Color figure can be viewed in the online issue, which is available at wileyonlinelibrary.com.]

longer emission maxima is then expected because of the preferred excitation of flavins. NADH can no longer be excited at laser wavelengths above 800 nm (Reinhardt et al., 2015). In our setup, using 780 nm of excitation reflected signal could be detected using a filter cube with a PBS (479 ± 40) nm and BP 445 ± 45 filters collect NADH and BP 535 ± 22 filters to detect FAD (data not shown).

CONCLUSIONS

Multiphoton microscopy provides a flexible and powerful tool for both *in situ* and *in vitro* studies of biological systems. Harmonic imaging microscopy is a relatively new imaging technique that allows visualization of biological structures with no need to include exogenous dyes/probes; even though it is currently under development, it has already encountered many applications. The simultaneous combination of second and THG yields structural details otherwise unattainable, such as those existing in multilayered structures or changes in nonlinear properties.

During the last two decades, nonlinear imaging techniques experienced an impressive growth in biological and biomedical imaging applications. New techniques have been developed and applied to several topics in modern biology and biomedical optics. Because each modality possesses its own strength and weakness in terms of detection sensitivity, molecular specificity, field of view, and penetration depth; the integration of two or more modalities on a single platform offers a tremendous opportunity to collect relevant information of processes occurring in the same sample at the same time point or interval. Such integration is especially important for the study of complex biological samples, in which multiple phenomena derive from the same stimulus.

By using a commercially standard confocal microscope, we have demonstrated how it can be adapted to integrate a multimodal workstation that comprises linear and nonlinear microscopic capabilities. The system offers the possibility to obtain brightfield, TPEF, SHG, THG, CARS, FLIM images and also to perform optical trapping. This is achieved by using components that can be readily inserted, attached, or appended externally to the confocal microscope, making the whole system very flexible to the user's needs. However, as mentioned above, only some techniques may be simultaneously accomplished. CARS can be only combined with SHG; and FLIM images needs to be done before or after the other techniques. This fact limits that some techniques can be carried out together in real time. However, our setup can perform brightfield imaging using forward scattered excitation light, allowing simultaneous brightfield and multiphoton images. Since both picture sets are generated from the same scanning process, there is a direct one to one correspondence between the brightfield and SHG/TPEF images and also a perfect superposition of these two/three imaging modalities is obtained. This helps a great deal in precisely locating the origin of SHG/TPEF in the biological specimen.

The current system has great potential and large room for prospective improvements. The THG signals could be more easily detected if longer wavelengths for excitation are used. This can be performed with new

laser sources, such InSight DeepSee introduced for Spectra-Physics. This new light source provides automated wavelength tuning through the entire relative transparency window of tissue (680–1300 nm) *in vivo*, delivers short femtosecond pulse width and integrates dispersion compensation in one easy-to-use package. Also, the laser can be configured with a second output, delivering femtosecond pulses at 1040 nm with an average power of 500 mW. Because both pulse trains are synchronized in time, they can be combined in a femtosecond CARS imaging setup to image, for example, lipids droplets via the CH_2 stretch vibrations at about 2840 cm^{-1}.

Our CARS configuration with two synchronized ps lasers, allows good spectral resolution, exhibiting excellent sensitivity and using less peak power at the focus compared with femtosecond's configuration [The photodamage in CARS microscopy increases with shorter wavelengths (Fu et al., 2006)]; however, it has the disadvantage of the cost and the need day-to-day alignment of temporal overlapping of the two beams. One alternative solution could be considered by using femtosecond OPO system to implement CARS because this can offers several advantages: all the pulses are inherently synchronized, which eliminates the alignment requirement; all the wavelengths are in the near IR region, and third, the fs pulses allow efficient generation of TPF, SHG, and THG signals.

Other aspect that we are planning to improve is the software compatibility. Presently, the software that operates the multiphoton systems, OTs and setup acquisition for FLIM options are independent and running in different computers. In the near future the software can be brought together into one single platform. One possibility that we are exploring to perform this, is using free software such as μ-Manager (the open source microscopy software). μ-Manager works with microscopes from all four major manufacturers (Leica, Nikon, Olympus and Zeiss), most scientific-grade cameras and many peripherals (stages, filter wheels, shutters, etc.) used in microscope imaging. This software has a simple and clean user interface, allowing execute common microscope image acquisition tasks such as time-lapses, multi-channel imaging, z-stacks, and combinations thereof. Together with the image processing application ImageJ, μManager provides a comprehensive, freely available, imaging solution for this kind of automation in multidimensional microscopy. This implementation would provide better synchrony and coherence among the systems, especially when it comes to defining a common region of interest, time lapse imaging, etc.

Although the data presented here demonstrate only a small subset of the capabilities of our platform for studies in reproductive biology, numerous other applications combined linear and NLO techniques do exist. In this article, we presented some practical applications of the developed platform in the field of prostate development, analysis of sperm cells, and ovary and breast cancer pathology. In cancer diagnosis, there is a need for development of a multimodal imaging-based diagnostic tool, to objectively evaluate morphological features with subcellular resolution and molecular compositions that are closely associated with tumor malignancy. Multi-modal microscopy can provide a powerful tool for investigating the dynamics of structure–function relationships at the molecular and subcellular levels. In combination with sophisticated animal models and computer-assisted data analysis, NLO microscopy techniques and image processing methods are opening new doors to the study of tumor biology, and facilitating the development of new strategies for early tumor diagnosis and treatment. Today, the application of multimodal nonlinear imaging is recognized in basic research in the biological and biomedical sciences, however regular applications in clinics are still rare, mainly because of their high cost and big size of the principal components. Therefore, especially technological improvements are required for miniaturization, improvement of the ease of handling and automated data processing and extraction of relevant information. An important step toward this goal is the modification of standard clinical endoscopes for multimodal nonlinear imaging suited for *in vivo* applications. The development of nonlinear optical endoscopy, which allows imaging under conditions in which a conventional nonlinear optical microscope cannot be used, will be the primary goal to extend applications of nonlinear optical microscopy toward clinical ones. There are several key challenges involved in the pursuit of *in vivo* nonlinear optical endoscopy. Between them, can be mentioned the necessity of obtain efficient ultrashort pulse laser liberations into a remote place, the need to enhance scan rates for monitoring biological processes and also, the miniaturization of the laser-scanning mechanisms to the millimeter scale. Finally, the design of a nonlinear optical endoscope based on micro-optics with great flexibility, and compact enough to be incorporated into endoscopes, will become an evolution of these microscopy approaches.

In summary, multimodal platforms like the one described here, are highly flexible and versatile, providing solutions for a large number of problems in the evolving area of bioimaging and will certainly contribute to the understanding of the reproductive system, in particular, and biomedicine, in general.

ACKNOWLEDGMENTS

The authors are also grateful to Dr. Gyselle Aguiar from Universidade Estadual de Ceará (Brazil) to providing sperm cells.

REFERENCES

Adur J, Pelegati VB, Costa LF, Pietro L, de Thomaz AA, Almeida DB, Bottcher-Luiz F, Andrade LA, Cesar CL. 2011. Recognition of serous ovarian tumors in human samples by multimodal nonlinear optical microscopy. J Biomed Opt 16:096017.

Adur J, Pelegati VB, de Thomaz AA, D'Souza-Li L, Assunção M, Bottcher-Luiz F, Andrade L, Cesar CL. 2012a. Quantitative changes in human epithelial cancers and osteogenesis imperfecta disease detected using nonlinear multicontrast microscopy. J Biomed Opt 17:081407.

Adur J, Pelegati VB, de Thomaz AA, Baratti MO, Almeida DB, Andrade LA, Bottcher-Luiz F, Carvalho HF, Cesar CL. 2012b. Optical biomarkers of serous and mucinous human ovarian tumor assessed with nonlinear optics microscopies. PLoS One 7:e47007.

Adur J, Carvalho HF, Cesar CL, Casco VH. 2014a. Nonlinear imaging microscopy: Methodological setup and applications for epithelial cancers diagnosis. In: Wilkins F, Editor. Nonlinear optics: Fundamentals, applications, and technological advances. New York: Nova Publishers. pp. 97–136.

Adur J, Pelegati VB, de Thomaz AA, Baratti MO, Andrade LA, Carvalho HF, Bottcher-Luiz F, Cesar CL. 2014b. Second harmonic

generation microscopy as a powerful diagnostic imaging modality for human ovarian cancer. J Biophotonics 7:37–48.
Adur J, Carvalho HF, Cesar CL, Casco VH. 2014c. Nonlinear optical microscopy signal processing strategies in cancer. Cancer Inform 13:67–76.
Antonioli E, Della-Colleta HHM, Carvalho H. 2004. Smooth muscle cell behavior in the ventral prostate of castrated rats. J. Androl 25: 50–56.
Antonioli E, Cardoso AB, Carvalho HF. 2007. Effects of long-term castration on the smooth muscle cell phenotype of the rat ventral prostate. J. Androl 28:777–783.
Ashkin A, Dziedzic JM, Bjorkholm JE, Chu S. 1986. Observation of a single-beam gradient force optical trap for dielectric particles. Opt Lett 11:288–290.
Augusto TM, Felisbino SL, Carvalho HF. 2008. Remodeling of rat ventral prostate after castration involves heparanase-1. Cell Tissue Res 332:307–315.
Barille R, Canioni L, Rivet S, Sarger L, Vacher P, Ducret T. 2001. Visualization of intracellular Ca^{2+} dynamics with simultaneous twophoton-excited fluorescence and third-harmonic generation microscopes. Appl Phys Lett 79:4045–4047.
Baron VT, Welsh J, Abedinpour P, Borgström P. 2011. Intravital microscopy in the mouse dorsal chamber model for the study of solid tumors. Am J Cancer Res 1:674–686.
Barzda V, Greenhalgh C, der Au JA, Elmore S, van Beek J, Squier J. 2005. Visualization of mitochondria in cardiomyocytes by simultaneous harmonic generation and fluorescence microscopy. Opt Express 13:8263–8276.
Bruni-Cardoso A, Vilamaior PSL, Taboga SR, Carvalho HF. 2008. Localized matrix metalloproteinase (MMP)−2 and MMP-9 activity in the rat ventral prostate during the first week of postnatal development. Histochem. Cell Biol 129:805–815.
Bruni-Cardoso A, Augusto TM, Pravatta H, Damas-Souza DM, Carvalho HF. 2010a. Stromal remodelling is required for progressive involution of the rat ventral prostate after castration: Identification of a matrix metalloproteinase-dependent apoptotic wave. Int. J. Androl 33:686–695.
Bruni-Cardoso A, Rosa-Ribeiro R, Pascoal VDB, De Thomaz AA, Cesar CL, Carvalho HF. 2010b. MMP-2 regulates rat ventral prostate development in vitro. Dev. Dyn 239:737–746.
Bruni-Cardoso A, Lynch CC, Rosa-Ribeiro R, Matrisian LM, Carvalho HF. 2010c. MMP-2 contributes to the development of the mouse ventral prostate by impacting epithelial growth and morphogenesis. Dev. Dyn 239:2386–2392.
Brustlein S, Ferrand P, Walther N, Brasselet S, Billaudeau C, Marguet D, Rigneault H. 2011. Optical parametric oscillator-based light source for coherent Raman scattering microscopy: Practical overview. J Biomed Opt 16:021106.
Campagnola PJ, Yuan Dong C. 2011. Second harmonic generation microscopy: Principles and applications to disease diagnosis. Laser Phot Rev 5:13–26.
Campagnola PJ, Wei MD, Lewis A, Loew LM. 1999. High-resolution nonlinear optical imaging of live cells by second harmonic generation. Biophys J 77:3341–3349.
Canioni L, Rivet S, Sarger L, Barille R, Vacher P, Voisin P. 2001. Imaging of Ca^{2+} intracellular dynamics with a third-harmonic generation microscope. Opt Lett 26:515–517.
Carriles R, Schafer DN, Sheetz KE, Field JJ, Cisek R, Barzda V, Sylvester AW, Squier JA. 2009. Imaging techniques for harmonic and multiphoton absorption fluorescence microscopy. Rev Sci Instrum 80:081101.
Carvalho HF, Taboga SR. 1996. Fluorescence and confocal laser scanning microscopy imaging of elastic fibers in hematoxylin-eosin stained sections. Histochem Cell Biol 106:587–592.
Cella F, Diaspro A. 2010. Two-photon excitation microscopy: A superb wizard for fluorescence imaging. In Diaspro A, editor. Nanoscopy and multidimensional optical fluorescence microscopy. Boca Raton, London: CRC Press. pp. 7.1–7.12.
Chen H, Wang H, Slipchenko MN, Jung Y, Shi Y, Zhu J, Buhman KK, Cheng JX. 2009. A multimodal platform for nonlinear optical microscopy and microspectroscopy. Opt Exp 17:1282–1290.
Cheng PC and Sun CK. 2006. Nonlinear (harmonic generation) optical microscopy. In: Pawley JB, editor. Handbook of biological confocal microscopy, 3rd ed. New York: Springer. pp. 703–721.
Chu SW, Chen IH, Liu TM, Chen PC, Sun CK, Lin BL. 2001. Multimodal nonlinear spectral microscopy based on a femtosecond Cr: forsterite laser. Opt Lett 26:1909–1911.
Chu SW, Chen SY, Tsai TH, Liu TM, Lin CY, Tsai HJ, Sun CK. 2003. In vivo developmental biology study using noninvasive multiharmonic generation microscopy. Opt Exp 11:3093–3099.
Conklin MW, Provenzano PP, Eliceiri KW, Sullivan R, Keely PJ. 2009. Fluorescence lifetime imaging of endogenous fluorophores in histopathology sections reveals differences between normal and tumor epithelium in carcinoma in situ of the breast. Cell Biochem Biophys 53:145–157.
Cox G, Moreno N, Feijó J. 2005. Second-harmonic imaging of plant polysaccharides. J Biomed Opt 10:024013.
Débarre D, Supatto W, Beaurepaire E. 2005. Structure sensitivity in third-harmonic generation microscopy. Opt Lett 30:2134–2136.
Denk W, Strickler JH, Webb WW. 1990. Two-photon laser scanning fluorescence microscopy. Science 248:73–76.
Evans CL, Potma EO, Puoris'haag M, Côté D, Lin CP, Xie XS. 2005. Chemical imaging of tissue in vivo with video-rate coherent anti-Stokes Raman scattering microscopy. Proc Natl Acad Sci USA 102: 16807–16812.
Ewald AJ, Brenot A, Duong M, Chan BS, Werb Z. 2008. Collective epithelial migration and cell rearrangements drive mammary branching morphogenesis. Dev. Cell 14:570–581.
Fu Y, Wang H, Shi R, Cheng JX. 2006. Characterization of photodamage in coherent anti-Stokes Raman scattering microscopy. Opt Exp 14:3942–3951.
Galla L, Meyer AJ, Spiering A, Sischka A, Mayer M, Hall AR, Reimann P, Anselmetti D. 2014. Hydrodynamic slip on DNA observed by optical tweezers-controlled translocation experiments with solid-state and lipid-coated nanopores. Nano Lett 14:4176–4182.
Gu M, Bird D, Day D, Fu L, Morrish D. 2010. Trapped-particle near-field scanning optical microscopy. In: Femtosecond Biophotonics. Core Technology and Applications. Cambridge, UK: Cambridge University Press. pp 116–148.
Gualda EJ, Filippidis G, Voglis G, Mari M, Fotakis C, Tavernarakis N. 2008. In vivo imaging of cellular structures in Caenorhabditis elegans by combined TPEF, SHG and THG microscopy. J Microsc 229:141–150.
Harper SA, Durrant BS, Russ KD, Bolamba D. 1998. Cryo-preservation of domestic dog epididymal sperm: A model for the preservation of genetic diversity. J Androl 19.
Heller I, Hoekstra TP, King GA, Peterman EJ, Wuite GJ. 2014. Optical tweezers analysis of DNA-protein complexes. Chem Rev 114: 3087–3119.
Huang S, Heikal AA, Webb WW. 2002. Two-photon fluorescence spectroscopy and microscopy of NAD(P)H and flavoprotein. Biophys J 82:2811–2825.
Huff TB, Cheng JX. 2007. In vivocoherent anti-Stokes Raman scattering imaging of sciatic nerve tissue. J. Microsc 225:175–182.
Khatibzadeh N, Stilgoe AB, Bui AA, Rocha Y, Cruz GM, Loke V, Shi LZ, Nieminen TA, Rubinsztein-Dunlop H, Berns MW. 2014. Determination of motility forces on isolated chromosomes with laser tweezers. Sci Rep 4:6866.
Kirkpatrick ND, Brewer MA, Utzinger U. 2007. Endogenous optical biomarkers of ovarian cancer evaluated with multiphoton microscopy. Cancer Epidemiol Biomarkers Prev 16:2048–2057.
König K, So PTC, Mantulin WW, Tromberg BJ, Gratton E. 1996. Two-photon excited lifetime imaging of autofluorescence in cells during UVA and NIR photostress. J Microsc 183:197–204.
Krafft C, Ramoji AA, Bielecki C, Vogler N, Meyer T, Akimov D, Rösch P, Schmitt M, Dietzek B, Petersen I, Stallmach A, Popp J. 2009. A comparative Raman and CARS imaging study of colon tissue. J Biophotonics 2:303–312.
Le TT, Huff TB, Cheng JX. 2009. Coherent anti-Stokes Raman scattering imaging of lipids in cancer metastasis. BMC Cancer 9:42.
Mathew M, Santos SI, Zalvidea D, Loza-Alvarez P. 2009. Multimodal optical workstation for simultaneous linear, nonlinear microscopy and nanomanipulation: Upgrading a commercial confocal inverted microscope. Rev Sci Instrum 80:073701.
Meyer T, Schmitt M, Dietzek B, Popp J. 2013. Accumulating advantages, reducing limitations: Multimodal nonlinear imaging in biomedical sciences—The synergy of multiple contrast mechanisms. J Biophotonics 6:887–904. Review.
Millard AC, Wiseman PW, Fittinghoff DN, Wilson KR, Squier JA, Müller M. 1999. Third-harmonic generation microscopy by use of a compact femtosecond fiber laser source. Appl Opt 38:7393–7397.
Miyata H, Noda N, Fairbairn DJ, Oldenbourg R, Cardullo RA. 2011. Assembly of the fluorescent acrosomal matrix and its fate in fertilization in the water strider, Aquarius remigis. J Cell Physiol 226: 999–1006.
Moreaux L, Sandre O, Blanchard-Desce M, Mertz J. 2000. Membrane imaging by simultaneous second-harmonic generation and two-photon microscopy. Opt Lett 25:320–322.
Moura DS, Silva DC, Williams AJ, Bezerra MA, Fontes A, de Araujo RE. 2015. Automatic real time evaluation of red blood cell elasticity by optical tweezers. Rev Sci Instrum 86:053702.

Mouras R, Rischitor G, Downes A, Salter D, Elfick A. 2010. Nonlinear optical microscopy for drug delivery monitoring and cancer tissue imaging. J. Raman Spectrosc 41:848–852.
Muller M, Squier J, Wilson KR, Brakenhoff GJ. 1998. 3D microscopy of transparent objects using third harmonic generation. J Microsc-Oxford 191:266–274.
Pelegati VB, Adur J, De Thomaz AA, Almeida DB, Baratti MO, Andrade LA, Bottcher-Luiz F, Cesar CL. 2012. Harmonic optical microscopy and fluorescence lifetime imaging platform for multimodal imaging. Microsc Res Tech 75:1383–1394.
Pesce G, Rusciano G, Sasso A, Isticato R, Sirec T, Ricca E. 2014. Surface charge and hydrodynamic coefficient measurements of Bacillus subtilis spore by optical tweezers. Colloids Surf B Biointerfaces 116:568–575.
Pesce G, Rusciano G, Zito G, Sasso A. 2015. Simultaneous measurements of electrophoretic and dielectrophoretic forces using optical tweezers. Opt Exp 23:9363–9368.
Plotnikov SV, Millard AC, Campagnola PJ, Mohler WA. 2006. Characterization of the myosin-based source for second-harmonic generation from muscle sarcomeres. Biophys J 90:693–703.
Prent N, Green C, Greenhalgh C, Cisek R, Major A, Stewart B, Barzda V. 2008. Intermyofilament dynamics of myocytes revealed by second harmonic generation microscopy. J Biomed Opt 13: 041318.
Provenzano PP, Eliceiri KW, Keely PJ. 2009. Multiphoton microscopy and fluorescence lifetime imaging microscopy (FLIM) to monitor metastasis and the tumor microenviroment. Clin Exp Metastasis 26:357–370.
Reinhardt K, Breunig HG, Uchugonova A, König K. 2015. Sperm metabolism is altered during storage by female insects: evidence from two-photon autofluorescence lifetime measurements in bedbugs. J R Soc Interface 12:0609.
Ribou A.C, Reinhardt K. 2012. Reduced metabolic rate and oxygen radicals production in stored insect sperm. Proc R Soc B 279:2196–2203.
Saager RB, Balu M, Crosignani V, Sharif A, Durkin AJ, Kelly KM, Tromberg BJ. 2015. In vivo measurements of cutaneous melanin across spatial scales: Using multiphoton microscopy and spatial frequency domain spectroscopy. J Biomed Opt 20:066005.
Scully RE, Young RH, Clement PB Eds,. 1998. Atlas of tumor pathology: Tumors of the ovary, maldeveloped gonads, fallopian tubes and broad ligament, 3rd ed. Washington, D.C.: Armed Forces Institute of Pathology.
Skala MC, Riching KM, Gendron-Fitzpatrick A, Eickhoff J, Eliceiri KW. 2007. In vivo multiphoton microscopy of NADH and FAD redox states, fluorescence lifetimes, and cellular morphology in precancerous epithelia. Proc Natl Acad Sci USA 104:19494–19499.
Spyratou E, Cunaj E, Tsigaridas G, Mourelatou EA, Demetzos C, Serafetinides AA, Makropoulou M. 2014. Measurements of liposome biomechanical properties by combining line optical tweezers and dielectrophoresis. J Liposome Res 9:1–9.
Squier J, Muller M, Brakenhoff G, Wilson KR. 1998. Third harmonic generation microscopy. Opt Exp 3:315–324.
Sun CK. 2005. Higher harmonic generation microscopy. Adv. Biochem Eng/Biotechnol 95:17–56.
Sun CK, Chu SW, Chen SY, Tsai TH, Liu TM, Lin CY, Tsai HJ. 2004. Higher harmonic generation microscopy for developmental biology. J Struct Biol 147:19–30.
Tang S, Zhou Y, Ju MJ. 2012. Multimodal optical imaging with multiphoton microscopy and optical coherence tomography. J Biophotonics 5:396–403.
Tilbury K, Campagnola PJ. 2015. Applications of second-harmonic generation imaging microscopy in ovarian and breast cancer. Perspect Medicin Chem 7:21–32.
Tsai MR, Shieh DB, Lou PJ, Lin CF, Sun CK. 2012. Characterization of oral squamous cell carcinoma based on higher-harmonic generation microscopy. J Biophotonics 5:415–424.
Vilamaior PS, Felisbino SL, Taboga SR, Carvalho HF. 2000. Collagen fiber reorganization in the rat ventral prostate following androgen deprivation: A possible role for smooth muscle cells. Prostate 45: 253–258.
Vilamaior PS, Taboga SR, Carvalho HF. 2005. Modulation of smooth muscle cell function: Morphological evidence for a contractile to synthetic transition in the rat ventral prostate after castration. Cell Biol. Int 29:809–816.
Williams RM, Flesken-Nikitin A, Ellenson LH, Connolly DC, Hamilton TC, Nikitin AY, Zipfel WR. 2010. Strategies for highresolution imaging of epithelial ovarian cancer by laparoscopic nonlinear microscopy. Transl. Oncol 3:181–194.
Yelin D, Oron D, Korkotian E, Segal M, Silberberg Y. 2002. Third-harmonic microscopy with a titanium sapphire laser. Appl Phys B Lasers O 74:S97–S101.
Zumbusch A, Holtom GR, Xie XS. 1999. Three-dimensional vibrational imaging by coherent anti-Stokes Raman scattering. Phys Rev. Lett 82:4142–4145.